STRUCTURAL, FERROELECTRIC AND PIEZOELECTRIC PROPERTIES OF PbTiO₃-MODIFIED COMPLEX $0.6Ba(Ti_{0.8}Zr_{0.2})O_3$-$0.4(Ba_{0.7}Ca_{0.3})TiO_3$ CERAMICS

Nguyen Huu Lam[1], Nguyen Hoang Thoan[1], Luong Thi Kim Phuong[2], Nguyen Xuan Duong[1,3], Luong Huu Bac[1], Dang Duc Dung[1]

Abstract: *In this paper, the structural and ferroelectric properties of PbTiO₃-modified $0.6Ba(Ti_{0.8}Zr_{0.2})O_3$-$0.4(Ba_{0.7}Ca_{0.3})TiO_3$ ceramics are reported. The nonlinear electric polarization is observed at room temperature in $0.6Ba(Ti_{0.8}Zr_{0.2})O_3$-$0.4(Ba_{0.7}Ca_{0.3})TiO_3$ and remained after the introduction of PbTiO₃. With increasing the PbTiO₃ concentration to 7 mol.%, high electrical remanent polarization of 13.11 μC/cm² is achieved. The large strain and S_{max}/E_{max} values were also obtained in PbTiO₃-modified compounds, where the highest piezoelectric coefficient values were estimated at around 642 pm/V for 3 mol.% PbTiO₃-addition into $0.6Ba(Ti_{0.8}Zr_{0.2})O_3$-$0.4(Ba_{0.7}Ca_{0.3})TiO_3$ compounds. We expected that the ceramics prepared in our study might be a suitable candidate for applications in electronic devices.*

1. Introduction

Recently, ferroelectric and piezoelectric ceramic materials have been widely used in electronic devices [1,2]. Among these materials, ferroelectric and piezoelectric perovskite-type ABO₃ are most commonly used. In PbTiO₃, the ferroelectric properties originated from hybridization between Pb and O atoms through covalence bonding Pb-O. While the interaction of Ba and oxygen as completely ionic Ba-O results in the ferroelectric properties of BaTiO₃ materials [3]. In another work, giant ferroelectric polarization is observed in tetragonal-like BiFeO₃ materials, which is related to a large strain-induced Fe-ion displacement relative to oxygen octahedra combined with the contribution of Bi $6s^2$ lone pair electrons [4]. Moreover, the B-site modification in perovskite structures, such as Hf⁴⁺ substitution for Ti⁴⁺ in BaTiO₃ cubic structure, is also reported as resulting in ferroelectricity [5]. In addition, in the report about complex ferroelectric oxide systems, Liu *et al.* [6] indicated the effect of the morphotropic phase

---

[1]Multifunctional Ferroics Materials Lab., School of Engineering Physics, Ha Noi University of Science and Technology; Email: dung.dangduc@hust.edu.vn

[2]Department of Postgraduate Training Management, Hong Duc University

[3]Department of Physics, University of Ulsan

boundary on the ferroelectric of materials. Whereby both ferroelectric polarization and the piezoelectric coefficient were enhanced due to the rotation of the direction of the polarization domain. Therefore, we can see that the A-site and B-site modification and morphotropic crystal symmetry in ABO$_3$ materials play an important role and could affect the ferroelectric of materials. Understanding the interaction and crystal symmetry of the materials will help improve and develop new ferroelectric materials for applications in electronic devices.

Lead-free ferroelectric materials $(1-x)$BaTiO$_3$+xBaZrO$_3$, the most promising system for replacing common commercial PbTiO$_3$, have recently attracted much attention because of their unique properties. When the BaZrO$_3$ concentration is below 10 mol.%, the compounds show traditional ferroelectric behavior, while a typical relaxor ferroelectric behavior is achieved with BaZrO$_3$ amounts to $0.26 \leq x \leq 0.4$ [7, 8]. With a small BaZrO$_3$ concentration of $0.03 \leq x \leq 0.08$, large unipolar strain levels of 0.18%-0.25% and remnant polarization of around 13-18 μC/cm^2 were obtained [9]. Moreover, BaTiO$_3$ materials co-modified with BaZrO$_3$ and CaTiO$_3$ had an excellent piezoelectric performance. Liu et $al.$ [10] reported a high piezoelectric coefficient $d_{33} \sim 690$ pC/N for 0.5Ba(Zr$_{0.2}$Ti$_{0.8}$)O$_3$ - 0.5(Ba$_{0.7}$Ca$_{0.3}$)TiO$_3$. In other work, the values of d_{33}=420 pC/N, k_p=57%, Q_m=120.2, and T_C=380 K and good thermal stability up to 370 K are also obtained for BaZrO$_3$ and CaTiO$_3$ co-modified BaTiO$_3$ materials [11]. The effect of morphotropic phase boundary on the ferroelectric and piezoelectric properties of (Ba,Ca)(Zr,Ti)O$_3$ materials has been reported. At the morphotropic phase boundary, the single-crystal of Ba(Ti$_{0.8}$Zr$_{0.2}$)TiO$_3$-(Ba$_{0.7}$Ca$_{0.3}$)TiO$_3$ composition shows giant d_{33} values of 1500-2000 pC/N and dynamic piezoelectric coefficient of 1.100 pm/V at 0.5 kV/mm, which is larger than that of Pb-based system (d_{33} of 300-600 pC/N) [12]. The large piezoelectric coefficients in Ba(Ti$_{0.8}$Zr$_{0.2}$)TiO$_3$-(Ba$_{0.7}$Ca$_{0.3}$)TiO$_3$ system is suggested to mainly occur at ferroelectric-ferroelectric phase transitions and rather small at a triple point or general phase convergence regions [13]. This suggests that controlling phase transition, as well as bonding, might be one of the important ways to develop advanced ferroelectric materials, widening new applications.

The crystal symmetry of complex $(1-x)$Ba(Ti$_{0.8}$Zr$_{0.2}$)TiO$_3$ +x(Ba$_{0.7}$Ca$_{0.3}$)TiO$_3$ materials is dependent on their composition. At room temperature, the materials were stable in a rhombohedral phase with x<0.4. While tetragonal phases were observed for x>0.52, an orthorhombic phase exists in the range of $0.44 \leq x \leq 0.51$. Especially, morphotropic phases were observed with x≈0.43 or 0.5 [13, 14]. Here, we used PbTiO$_3$ materials, exhibiting the tetragonal structure at room temperature, to modify 0.6Ba(Ti$_{0.8}$Zr$_{0.2}$)TiO$_3$-0.4(Ba$_{0.7}$Ca$_{0.3}$)TiO$_3$ materials. We expect that the Pb-substitution at complex A-sites, as well as complex dependence of crystal symmetry on the composition of (Ba,Ca)(Zr,Ti)O$_3$ materials, will show interesting ferroelectric and piezoelectric properties.

In this work, we successfully fabricated PbTiO$_3$-modified 0.6Ba(Ti$_{0.8}$Zr$_{0.2}$)O$_3$-0.4(Ba$_{0.7}$Ca$_{0.3}$)TiO$_3$ compound by conventional solid-state synthesis. The ferroelectric properties of samples were investigated. Meanwhile, bipolar and unipolar piezoelectric responses showed the largest strain (0.321%) and piezoelectric coefficient (642 pm/V) in the sample with 3 mol.% PTO addition. The PbTiO$_3$-modified complex [0.6Ba(Ti$_{0.8}$Zr$_{0.2}$)TiO$_3$-0.4(Ba$_{0.7}$Ca$_{0.3}$)TiO$_3$] compounds exhibited an increase in the maxima polarization from 21.82 μC/cm^2 to 23.37 μC/cm^2.

2. The Experimental

2.1. Sample preparation

In this work, 0.6Ba(Ti$_{0.8}$Zr$_{0.2}$)O$_3$-0.4(Ba$_{0.7}$Ca$_{0.3}$)TiO$_3$ (named as BTO64) and ceramic samples with the compositions of (1-x)[0.6Ba(Ti$_{0.8}$Zr$_{0.2}$)O$_3$-0.4(Ba$_{0.7}$Ca$_{0.3}$)TiO$_3$] + xPbTiO$_3$ (named as BTO64-xPTO, x=0.5, 1, 3, 5, 7, and 9 mol.%) were synthesized by conventional solid-state method. Analytical-grade metal oxides or carbonate powders: BaCO$_3$, ZrO$_2$, TiO$_2$, CaCO$_3$, and PbO were used as received. First, all the powders were weighed in a mole percentage according to the nominal compositions and mixed by ball milling in alcohol using zirconia balls for 24 hrs. Then, they were dried and calcined in air at 1100°C for 8 hrs. After the calcination, the powders were ground, ball-milled again for 24 hrs, and then dried. After drying, the mixtures were ground and mixed with 5 wt.% polyvinyl alcohol added as a binder, pressed into pellets under 98 MPa. The resultant pellets were finally sintered at 1350°C for 6 hrs. The sample fabrication processes are summarized in Fig.1.
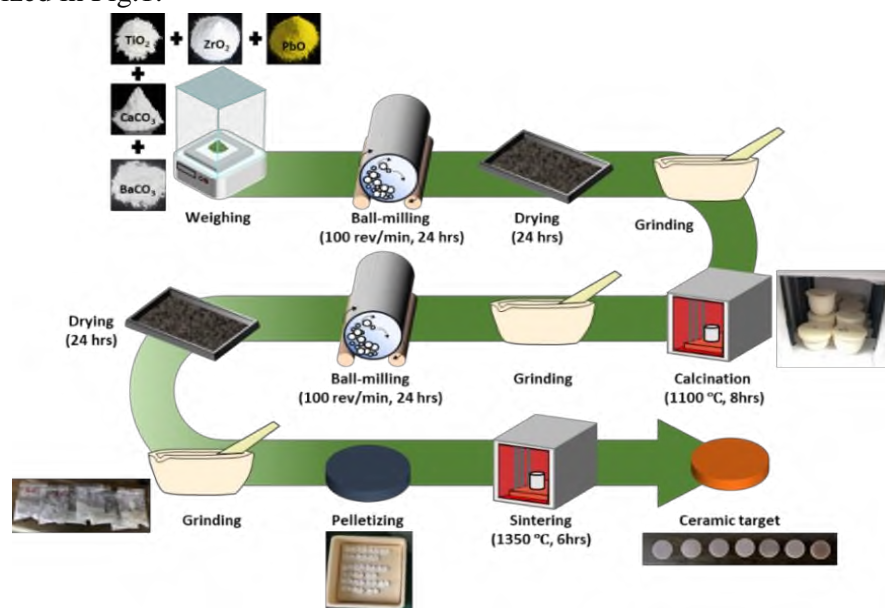
Fig.1. *Process workflows for BTO64 and BTO64-xPTO (x= 0.5, 1, 3, 5, 7, and 9 mol.%) materials*

2.2. Sample characterization

The crystal structure of the samples was confirmed by X-ray diffraction measurements (XRD, Brucker D8 Advance). For further structural analysis, Raman spectra were obtained using a Renishaw in Via Micro Raman Microscope system. For the ferroelectric measurements, pellet's surfaces were polished and then covered with silver electrodes on both sides and heated at 800°C for 30 min in the air. Polarization vs. electric field (*P-E*) hysteresis loops, field-induced strain (*S-E*) hysteresis loops were recorded by a Precision LC II ferroelectric test system (Radiant Technologies. Inc.).

3. Results and discussion

The XRD patterns of BTO64 and BTO64-*x*PTO (*x*= 0.5, 1, 3, 5, 7, 9 mol.%) samples were shown in Fig. 2(A). All samples exhibit perovskite structures without a second phase being detected, which agrees with JCPDS card no 05-0626 and 85-0368. To determine phases, the (002)/(200) and (202)/(220) characteristic peaks are de-convoluted, as shown in Fig. 2(B) and (C), respectively. The splitting of (002)/(200) and (202)/(220) peaks indicated the existence of tetragonal and rhombohedral phases, respectively. It can be seen that BTO64 possesses a rhombohedral phase, characterized by a single (200) peak and a double (202)/(220) peak. With the addition of $PbTiO_3$, both (002)/(200) and (202)/(220) peaks split, which suggests BTO64-*x*PTO (*x*= 0.5, 1, 3, 5, 7, 9 mol.%) samples stabilize in a polycrystalline perovskite structure along with the coexistence of tetragonal and rhombohedral phases.

The XRD patterns are magnified to 2θ-range of 30°-33° for satellite peaks (101)/(110) (Fig.2(D)), suggesting the effects of PTO on the crystal structure of the BTO64. When the concentration of PTO is up to 1 mol.%, the peak position tends to shift to lower diffraction angles, provided that the lattice parameter of BTO64 is expanded. In contrast, at the PTO concentrations higher than 1 mol.%, these peaks shift to higher angles, indicating compression of lattice parameters. The results showed that BTO-*x*PTO has complex distortion in lattice parameters. The lattice distortion of BTO64-*x*PTO could be explained by considering the radii difference between impurity and host cations. Shannon *et al.* [15] reported that the radii of Ba^{2+} and Ca^{2+} cations (in the coordination number of XII) are 1.61 Å and 1.34 Å, respectively. At the same coordination number of XII, the radius of Pb^{2+} cations is 1.49 Å. Therefore, the substitution of Pb^{2+} at the *A*-sites of the BTO64 results in complex lattice distortion. The lattice could be compressed when Pb^{2+} cations are substituted Ba-sites because Pb^{2+} cations are smaller than Ba^{2+} cations. However, the lattice might be expanded when Pb^{2+} is substituted on the Ca-sites. The observed lattice distortion and the shift of diffraction peaks suggest that the Pb^{2+} cations are mainly substituted at Ba-sites at low PTO addition. With the lattice expansion in BTO64 crystal, the lattice energy of host BTO64 materials will increase. Thus, further

PTO addition into host BTO64 materials is selected to decrease the lattice energy of host BTO64 crystals via random contribution at Ca-sites. Further investigation is needed to understand the precise origin of lattice distortion in BTO64-xPTO materials.
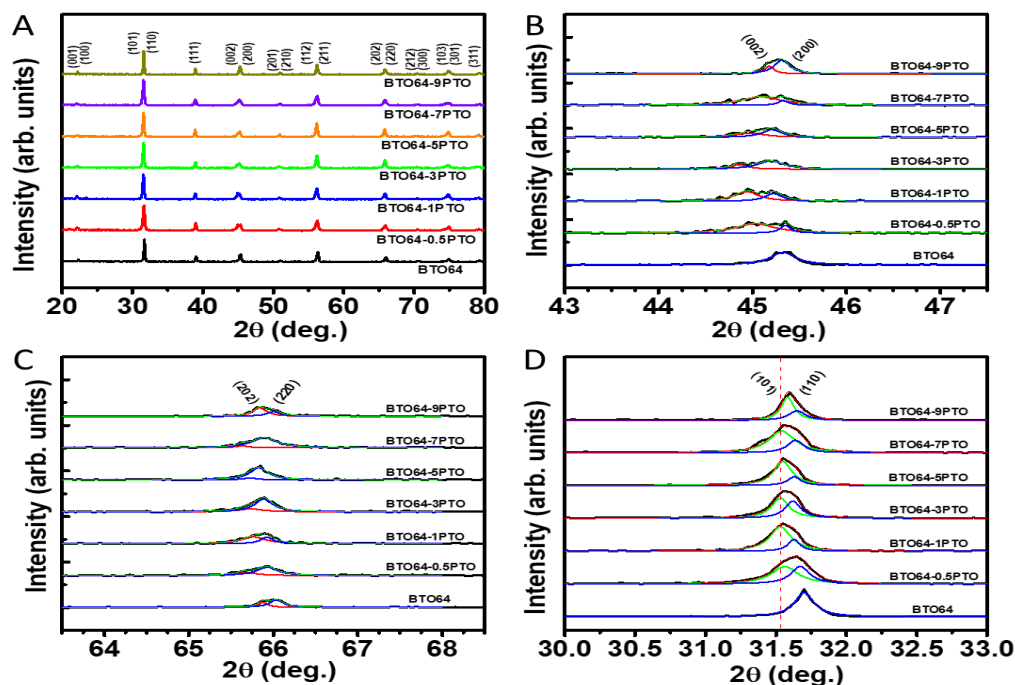
Fig.2. *(A) X-ray diffraction patterns, (B,C) de-convoluted XRD patterns of (002)/(200) and (202)/(220) peaks, respectively, and (D) magnification of X-ray patterns in the 2θ range of 30-33° of BTO64 and BTO64-xPTO (x= 0.5, 1, 3, 5, 7, and 9 mol%)*

A more detailed structural study was probed by Raman scattering. Fig. 3(A) shows the Raman spectra of the BTO64 and BTO64-xPTO samples. The shape of Raman spectra remains unchanged, confirming that no impurity-related phase appeared. It is reported that the vibration modes of the tetragonal structure BTO consisting of $4E(TO + LO) + 3A_1(TO + LO) + B_1(TO + LO)$ modes, with A_1 mode and E mode, have both Raman activity and infrared activity, B_1 only Raman activity [16]. Raman peaks assigned to the fundamental TO, LO modes of A_1, and E symmetries were shown in Fig. 3(B) for BTO64 and BTO64-xPTO (x= 3 and 9 mol.%), which is in agreement with recent reports [16-20]. The observation of $E(LO_2)$ and B_1; $E(LO_4)$ and $A_1(LO_3)$ modes around 294 cm^{-1} and 728 cm^{-1}, respectively, is the signature of the tetragonal structure of BTO [21], further confirmed our XRD results. The signals in 150–330 cm^{-1} were attributed to the O-Ti-O bending and A-O vibration modes [22]. Raman active vibration modes are $E(TO_2)$ at 217 cm^{-1}; $A_1(LO_1)$ at 236 cm^{-1}; $A_1(TO_2)$ at 260 cm^{-1}; and $E(LO_2)$ and B_1 at 294 cm^{-1}. The $E(LO_2)$ and B_1 modes are associated with asymmetric TiO_6 octahedra, suggesting a tetragonal distortion in the octahedral coordination of Ti atoms [23, 24]. The $E(TO_4)$ and $E(LO_3)$ modes at approximately 521 cm^{-1} correspond to the torsion modes of Ti-O, while

$A_1(TO_3)$ mode (~548 cm^{-1}) was related to the vibration displacement of oxygen atoms [22, 25]. Whereas the peak at 794 cm^{-1} corresponded to A_{1g} mode, it could be associated with a breathing mode of BO_6 octahedra related to A- or B-site substitutions in the perovskite structure [17, 26].
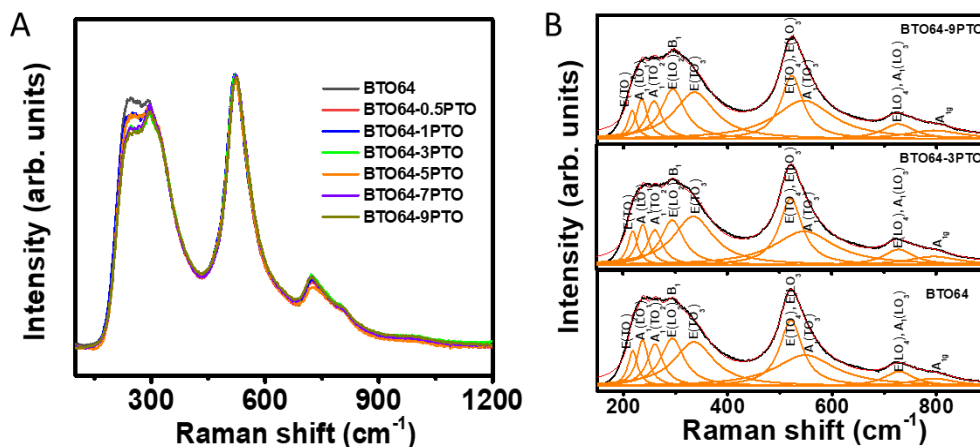

Fig.3. *(A) Raman spectra at room temperature of the BTO64 and BTO-xPTO, (B) deconvolutions of the Raman spectra of the BTO64 and BTO-3PTO and BTO-9PTO*

The polarization vs. electric field (*P-E*) hysteresis loops for BTO64 and BTO64-*x*PTO samples with *x*=0.5, 1, 3, 5, 7, and 9 mol.%, was shown in Fig. 4(A)-(G), respectively. The presence of well-defined *P-E* hysteresis loops for all samples confirms their ferroelectric nature. In addition, all samples exhibited unsaturated polarization under an external electrical field at room temperature, likely deriving from surface and impurity defects. The large surface area with defects could induce low conductivity and increase leakage current [27]. Because of leakage current, it is not easy to polarize the samples to a high electric field. The electrical remanent polarization (P_r) and coercive field (E_C) of the BTO64 were estimated at around 10.46 μC/cm^2 and 2.41 kV/mm, respectively. With BTO64-*x*PTO samples, the P_r and E_C values had complex dependence on the PTO concentration. The lower P_r values compared to that of the BTO64 sample were obtained in BTO-*x*PTO with *x*=1, 3, and 9 mol.%. The highest P_r value was observed in the BTO64-7PTO sample, with $P_r \approx 13.11$ μC/cm^2 and $E_C \approx 7.02$ kV/mm (Fig. 4(F)). The P_r values varried from 6.18 to 13.11 μC/cm^2, while the E_C values were from 3.07 to 7.79 kV/mm (detail is shown in Table 1). Based on the grain size of the samples, the changed polarization remanence and coercive electrical field could be explained [28, 29]. For ferroelectrics, the proportion of grains contributing to polarization reverse can be expressed as $f = f_0|1 - \exp(-G_a d^3/kT)|$ with G_a being a constant and representing the grain anisotropy energy density and *d* being the grain size. Thus, *f* is relevant only with the grain size *d*. The number of grains contributing to polarization reverses increases with the increasing grain size, giving rise to the enhancement of the ferroelectricity and vice versa.
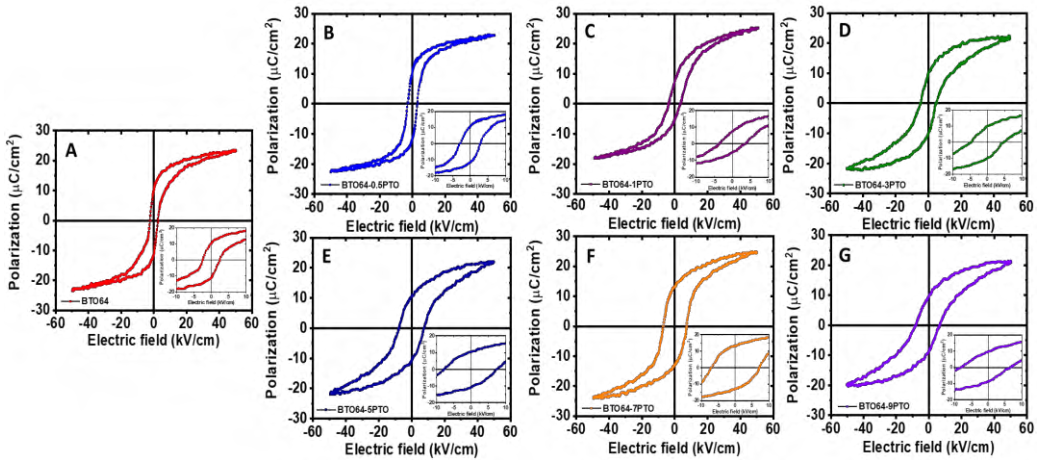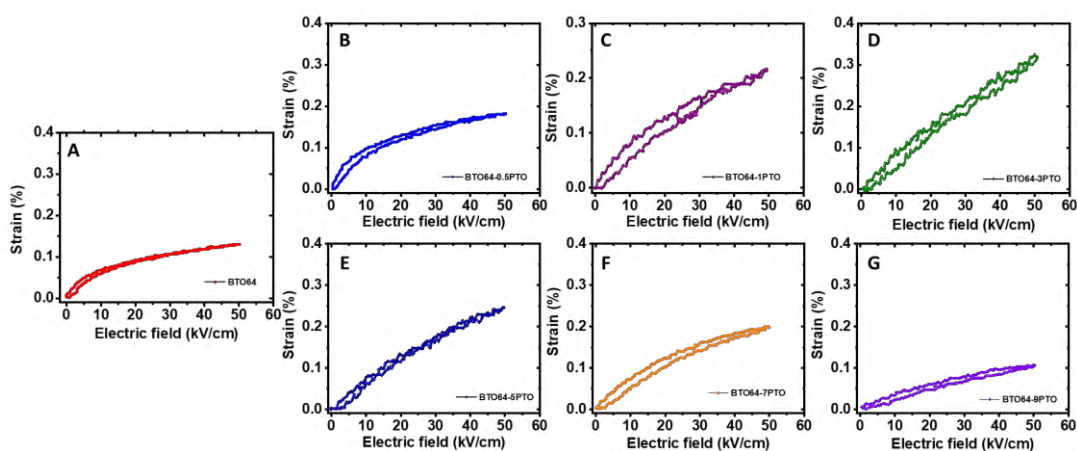
Fig.4. *The polarization hysteresis loop at room temperature of (A) BTO64, and BTO64-xPTO with various of x concentrations: (B) 0.5 mol.%, (C) 1 mol.%, (D) 3 mol.%, (E) 5 mol.%, (F)7 mol.%, and (G) 9 mol.%. The inset of each figure shows the magnified P-E curve at a low applied electric field*

Figures 5 and 6 show the bipolar and unipolar strain (S-E) curves of BTO64 and BTO64-xPTO. It is known that the total strain in piezoelectric ceramics is mainly attributed to the combined effect of piezoelectricity and electrostriction [30]. All samples show typical butterfly-shaped bipolar strain curves and behavior like ferroelectric ceramics. For the BTO64 sample, the obtained strain value is 0.129% (Fig. 5(A) and 6(A)). With the PTO concentration up to 9 mol.%, the strain hysteresis is relatively slim, and smaller strains (0.106%) are achieved (as shown in Fig. 5(G) and 6(G)). The highest strain value (0.321%) is obtained in the BTO64-3PTO sample (Fig. 5(D) and 6(D)). The BTO64-3PTO sample shows a high piezoelectric coefficient of 642 pm/V, much higher than pure BTO64 (258 pm/V). The results are well consistent with the ferroelectric state as shown in *P-E* hysteresis loops. The summarization of values is shown in Table 1.
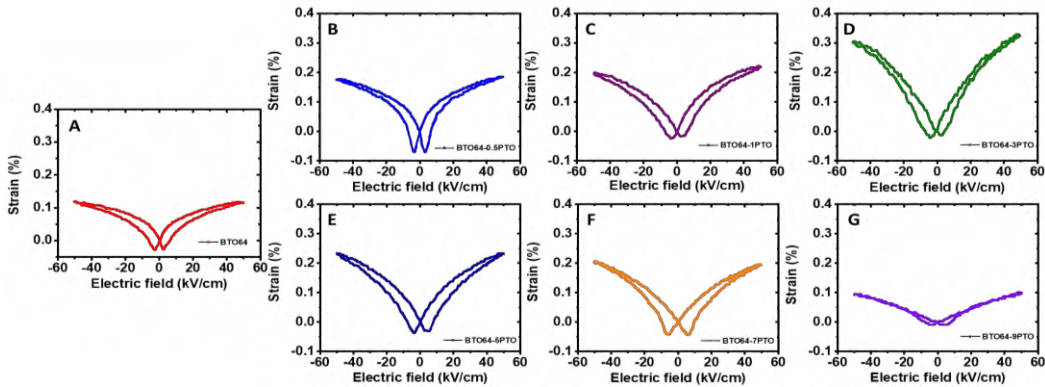
Fig.5. *The bipolar electric field induced strain hysteresis loops of (A) BTO64, and BTO64-xPTO with various PTO concentrations: (B) 0.5 mol.%, (C) 1 mol.%, (D) 3 mol.%, (E) 5 mol.%, (F)7 mol.%, and (G) 9 mol.%*

Fig.6. *The unipolar electric field-induced strain hysteresis loops of (A) BTO64, and BTO64-xPTO with various PTO concentrations: (B) 0.5 mol.%, (C) 1 mol.%, (D) 3 mol.%, (E) 5 mol.%, (F)7 mol.%, and (G) 9 mol.%*

Table 1. *The strain, S_{max}/E_{max}, P_m, P_r, and E_C values for BTO64 and BTO64-xPTO (x = 0.5, 1, 3, 5, 7, and 9 mol.%)*

Compositions $(1-x)[0.6Ba(Ti_{0.8}Zr_{0.2})O_3-0.4(Ba_{0.7}Ca_{0.3})TiO_3]+xPbTiO_3$	Sample name	Strain (%)	S_{max}/E_{max} (pm/V)	P_m ($\mu C/cm^2$)	P_r ($\mu C/cm^2$)	E_C (kV)
$[0.6Ba(Ti_{0.8}Zr_{0.2})O_3+0.4(Ba_{0.7}Ca_{0.3})TiO_3]$	BTO64	0.129	258	23.28	10.46	2.41
$0.995[0.6Ba(Ti_{0.8}Zr_{0.2})O_3+0.4(Ba_{0.7}Ca_{0.3})TiO_3]+0.005PbTiO_3$	BTO64-0.5PTO	0.181	362	22.79	10.72	3.07
$0.99[0.6Ba(Ti_{0.8}Zr_{0.2})O_3+0.4(Ba_{0.7}Ca_{0.3})TiO_3]+0.01PbTiO_3$	BTO64-1PTO	0.216	432	21.64	6.18	3.52
$0.97[0.6Ba(Ti_{0.8}Zr_{0.2})O_3+0.4(Ba_{0.7}Ca_{0.3})TiO_3]+0.03PbTiO_3$	BTO64-3PTO	0.321	642	21.81	10.07	4.71
$0.95[0.6Ba(Ti_{0.8}Zr_{0.2})O_3+0.4(Ba_{0.7}Ca_{0.3})TiO_3]+0.05PbTiO_3$	BTO64-5PTO	0.248	496	21.84	10.52	7.79
$0.93[0.6Ba(Ti_{0.8}Zr_{0.2})O_3+0.4(Ba_{0.7}Ca_{0.3})TiO_3]+0.07PbTiO_3$	BTO64-7PTO	0.198	396	24.72	13.11	7.02
$0.91[0.6Ba(Ti_{0.8}Zr_{0.2})O_3+0.4(Ba_{0.7}Ca_{0.3})TiO_3]+0.09PbTiO_3$	BTO64-9PTO	0.106	212	21.03	8.39	6.87

3. Conclusions

The ferroelectric $PbTiO_3$-modified $0.6Ba(Ti_{0.8}Zr_{0.2})O_3+0.4(Ba_{0.7}Ca_{0.3})TiO_3$ ceramics were successfully synthesized by the conventional solid-state method. The

good incorporation of $PbTiO_3$ into the $0.6Ba(Ti_{0.8}Zr_{0.2})O_3+0.4(Ba_{0.7}Ca_{0.3})TiO_3$ host lattices resulted in lattice parameter distortion. The BTO64-7PTO shows high electrical remanent polarization of 13.11 $\mu C/cm^2$. The coefficient electric field values increase from 2.41 to 7.79 kV with 5 mol.% $PbTiO_3$ addition. The large strain and S_{max}/E_{max} values were also observed in $PbTiO_3$-modified compounds. The observed ferroelectric properties in these compounds are expected to produce new material for current applications in electronic devices.

Declaration of Competing Interest

The authors declare that they have no known competing financial interests or personal relationships that could have appeared to influence the work reported in this paper.

Acknowledgment

References

[1]   H. Wei, H. Wang, Y. Xia, D. Cui, Y. Shi, M. Dong, C. Liu, T. Ding, J. Zhang, Y. Ma, N. Wang, Z. Wang, Y. Sun, R. Wei, and Z. Guo (2018), An overview of lead-free piezoelectric materials and devices, *J. Mater. Chem.* C(6),12446–12467. https://doi.org/10.1039/C8TC04515A.

[2]   J. Hao, W. Li, J. Zhai, and H. Chen (2019), Progress in high-strain perovskite piezoelectric ceramics, *Mater. Sci. Eng. R Rep.* 135, 1–57. https://doi.org/10.1016/j.mser.2018.08.001

[3]   R. E. Cohen (1992), Origin of ferroelectricity in perovskite oxides, *Nature*, 358, 136-138. https://doi.org/10.1038/358136a0

[4]   J. X. Zhang, Q. He, M. Trassin, W. Luo, D. Yi, M. D. Rossell, P. Yu, L. You, C. H. Wang, C. Y. Kuo, J. T. Heron, Z. Hu, R. J. Zeches, H. J. Lin, A. Tanaka, C. T. Chen, L. H. Tjeng, Y. H. Chu, and R. Ramesh (2011), Microscopic origin of the giant ferroelectric polarization in tetragonal-like $BiFeO_3$, *Phys. Rev. Lett.* 107, 147602. https://doi.org/10.1103/PhysRevLett.107.147602

[5]   A. Sati, P. Pokhriyal, A. Kumar, S. Anwar, A. Sagdeo, N. P. Lalla, and P. R. Sagdeo (2021), Origin of ferroelectricity in cubic phase of Hf substituted $BaTiO_3$, *J. Phys.: Condens. Matter*, 33, 165403. https://doi.org/10.1088/1361-648X/abf0bf

[6]   W. Liu, and X. Ren (2009), Large Piezoelectric Effect in Pb-Free Ceramics, *Phys. Rev. Lett.* 103, 257602. https://doi.org/10.1103/PhysRevLett.103.257602

[7]   Z. Yu, R. Guo, A. S. Bhalla (2000), Dielectric behavior of $Ba(Ti_{1-x}Zr_x)O_3$ single crystals, *J. Appl. Phys.* 88, 410. https://doi.org/10.1063/1.373674

[8]   J. Bera, S. K. Rout (2005), On the formation mechanism of $BaTiO_3$–$BaZrO_3$ solid solution through solid-oxide reaction, *Mater. Lett.* 59, 135–138. https://doi.org/10.1016/j.matlet.2004.07.053

[9]   Z. Yu, C. Ang, R. Guo, A. S. Bhalla (2002), Piezoelectric and strain properties of $Ba(Ti_{1-x}Zr_x)O_3$ ceramics, *J. Appl. Phys.* 92, 1489-1493. https://doi.org/10.1063/1.1487435

[10]   W. Liu, X. Ren (2009), Large piezoelectric effect in Pb-free ceramics, *Phys. Rev. Lett.* 103, 257602. https://doi.org/10.1103/PhysRevLett.103.257602

[11]   L. Liu, S. Zheng, Y. Huang, D. Shi, S. Wu, L. Fang, C. Hu, and B. Elouadi (2012), Structure and piezoelectric properties of $(1 - 0.5x)BaTiO_3$–$0.5x(0.4BaZrO_3 - 0.6CaTiO_3)$ ceramics, *J. Phys. D: Appl. Phys.* 45, 295403. http://dx.doi.org/10.1088/0022-3727/45/29/295403

[12]   T. R. Shrout and S. J. Zhang (2007), Lead-free piezoelectric ceramics: Alternatives for PZT?, *J. Electroceram.* 19, 113-126. https://doi.org/10.1007/s10832-007-9047-0

[13]   M. Acosta, N. Novak, W. Jo, and J. Rodel (2014), Relationship between electromechanical properties and phase diagram in the $Ba(Zr_{0.2}Ti_{0.8})O_3$–$x(Ba_{0.7}Ca_{0.3})TiO_3$ lead-free piezoceramic, *Acta Mater.* 80, 48-55. https://doi.org/10.1016/j.actamat.2014.07.058

[14]   T. Yang, X. Ke, and Y. Wang (2016), Mechanisms Responsible for the Large Piezoelectricity at the Tetragonal-Orthorhombic Phase Boundary of $(1-x)BaZr_{0.2}Ti_{0.8}O_3$-$xBa_{0.7}Ca_{0.3}TiO_3$ System, *Sci. Rep.* 6, 33392. https://doi.org/10.1038/srep33392

[15]   R. D. Shannon (1976), Revised effective ionic radii and systematic studies of interatomic distances in halides and chalcogenides, *Acta. Cryst.* A 32, 751-767. https://doi.org/10.1107/S0567739476001551

[16]   T. Badapanda, V. Senthil, S. Panigrahi, and S. Anwar (2013), Diffuse phase transition behavior of dysprosium doped barium titanate ceramic, J. Electroceram. 31, 55-60. https://doi.org/10.1007/s10832-013-9808-x

[17]   V. Vinothini, B. Vaidhyanathan, J. Binner (2011), Microwave assisted synthesis of barium zirconium titanate nanopowders, *J. Mater. Sci.* 46, 2155-2161. https://doi.org/10.1007/s10853-010-5052-9

[18]   Z. Abdelkafi, G. Khasskhoussi, N. Abdelmoula, and H. Khemakhem (2015), Ferroelectric, piezoelectric and Raman spectroscopy studies of $BaTi_{0.925}(Nb_{0.5}Yb_{0.5})_{0.075}O_3$ ceramic, *Ceram. Int.* 41, 14839–14844. https://doi.org/10.1016/j.ceramint.2015.08.011

[19]   M. Singh, B.C. Yadav, A. Ranjan, M. Kaur, and S.K. Gupta (2017), Synthesis and characterization of perovskite barium titanate thin film and its application as LPG sensor, *Sen. Act.* B 241, 1170-1178. http://dx.doi.org/10.1016%2Fj.snb.2016.10.018

[20]   R. Kumar, K. Asokan, S. Patnaik, and B. Birajdar (2018), Combined effect of oxygen annealing and La-doping in broadening the phase transition of $Ba(Zr_{0.2}Ti_{0.8})O_3$ ceramics, *J. Alloys Compound.* 737, 561-567. https://doi.org/10.1016/j.jallcom.2017.11.344

[21] H. Hayashi, T. Nakamura, and T. Ebina (2013), In-situ Raman spectroscopy of BaTiO3 particles for tetragonal–cubic transformation, *J. Phys. Chem. Solids* 74, 957-962. https://doi.org/10.1016/j.jpcs.2013.02.010

[22] M. I. Aroyo, A. Kirov, C. Capillas, J. M. Perez-Mato, and H. Wondratschek (2006), Bilbao Crystallographic Server. II. Representations of crystallographic point groups and space groups, *Acta Cryst. Sect.* A 62, 115-128. https://doi.org/10.1107/S0108767305040286

[23] K. Momma and F. Izumi (2011), VESTA 3 for three-dimensional visualization of crystal, volumetric and morphology data, *J. Appl. Cryst.* 44, 1272-1276. https://doi.org/10.1107/S0021889811038970

[24] A. E. Souza, S. R. Teixeira, C. Morilla-Santos, W. H. Schreiner, P. N. L. Filho, and E. Longo (2014), Photoluminescence activity of $Ba_{1-x}Ca_xTiO_3$: dependence on particle size and morphology, *J. Mater. Chem.* C 2, 7056-7070. https://doi.org/10.1039/C4TC00897A

[25] T. Mondal, S. Das, T. Badapanda, T. P. Sinha and P. M. Sarun (2017), Effect of Ca^{2+} substitution on impedance and electrical conduction mechanism of $Ba_{1-x}Ca_xZr_{0.1}Ti_{0.9}O_3$ ($0.00 \leq x \leq 0.20$) ceramics, *Phys. B*, 508, 124-135. https://doi.org/10.1016/j.physb.2016.12.021

[26] V. Buscaglia, S. Tripathi, V. Petkov, M. Dapiaggi, M. Deluca, A. Gajović, and Y. Ren (2014), Average and local atomic-scale structure in $BaZr_xTi_{1-x}O_3$ (x = 0.10, 0.20, 0.40) ceramics by high-energy x-ray diffraction and Raman spectroscopy, *J. Phys. Cond. Matter.* 26, 065901. http://dx.doi.org/10.1088/0953-8984/26/6/065901

[27] C. Mathieu, C. Lubin, G. L. Doueff, M. Cattelan, P. Gemeiner, B. Dkhil, E. K. H. Salje, and N. Barrett (2018), Surface proximity effect, imprint memory of ferroelectric twins, and tweed in the paraelectric phase of $BaTiO_3$, *Sci. Rep.* 8, 13660. https://doi.org/10.1038/s41598-018-31930-4

[28] H. Orihara, S. Hashimoto, and Y. Ishibashi (1994), A theory of D-E hysteresis loop based on the avrami model, *J. Phys. Soc. Jpn.* 63, 1031. https://doi.org/10.1143/JPSJ.63.1031

[29] E. V. Ramana, F. Figueiras, A. Mahajan, D. M. Tobaldi, B. F. O. Costa, M. P. F. Graca, and M. A. Valente (2016), Effect of Fe-doping on the structure and magnetoelectric properties of $(Ba_{0.85}Ca_{0.15})(Ti_{0.9}Zr_{0.1})O_3$ synthesized by a chemical route, *J. Mater. Chem.* C 4, 1066-1079. https://doi.org/10.1039/C5TC00914F

[30] J. Hao, W. Li, J. Zhai, and H. Chen (2019), Progress in high-strain perovskite piezoelectric ceramics, *Mater. Sci. Eng. R Rep.* 135, 1-57. https://doi.org/10.1016/j.mser.2018.08.001